



# From Naked Spheroids to Disky Galaxies: How Do Massive Disk Galaxies Shape Their Morphology?

Luca Costantin<sup>1,2</sup> , Pablo G. Pérez-González<sup>1,3</sup> , Jairo Méndez-Abreu<sup>4,5</sup> , Marc Huertas-Company<sup>4,5,6</sup> ,  
Belén Alcalde Pampliega<sup>7</sup> , Marc Balcells<sup>4,5,8</sup> , Guillermo Barro<sup>9</sup> , Daniel Ceverino<sup>10,11</sup> , Paola Dimauro<sup>12</sup>,  
Helena Domínguez Sánchez<sup>13,14</sup> , Néstor Espino-Briones<sup>15</sup> , and Anton M. Koekemoer<sup>16</sup>

<sup>1</sup> Centro de Astrobiología (CSIC-INTA), Ctra de Ajalvir km 4, Torrejón de Ardoz, E-28850, Madrid, Spain; [lcostantin@cab.inta-csic.es](mailto:lcostantin@cab.inta-csic.es)

<sup>2</sup> INAF-Osservatorio Astronomico di Brera, Via Brera 28, I-20121, Milano, Italy

<sup>3</sup> Honorary Professor, Departamento de Física de la Tierra y Astrofísica, Facultad de CC. Físicas, Universidad Complutense de Madrid, E-28040 Madrid, Spain

<sup>4</sup> Instituto de Astrofísica de Canarias, E-38200, La Laguna, Tenerife, Spain

<sup>5</sup> Departamento de Astrofísica, Universidad de La Laguna, E-38205, La Laguna, Tenerife, Spain

<sup>6</sup> LERMA, Observatoire de Paris, CNRS, PSL, Université de Paris, France

<sup>7</sup> European Southern Observatory (ESO), Alonso de Córdova 3107, Vitacura, Casilla 19001, Santiago de Chile, Chile

<sup>8</sup> Isaac Newton Group of Telescopes, Apartado 321, E-38700, Santa Cruz de La Palma, Islas Canarias, Spain

<sup>9</sup> Department of Physics, University of the Pacific, 3601 Pacific Ave., Stockton, CA 95211, USA

<sup>10</sup> Universidad Autónoma de Madrid, Ciudad Universitaria de Cantoblanco, E-28049, Madrid, Spain

<sup>11</sup> CIAFF, Facultad de Ciencias, Universidad Autónoma de Madrid, E-28049 Madrid, Spain

<sup>12</sup> Observatório Nacional, Rua General José Cristino, 77, São Cristóvão, 20921-400, Rio de Janeiro, Brazil

<sup>13</sup> Institute of Space Sciences (ICE, CSIC), Campus UAB, Carrer de Magrans, E-08193, Barcelona, Spain

<sup>14</sup> Institut d'Estudis Espacials de Catalunya (IEEC), E-08034, Barcelona, Spain

<sup>15</sup> Instituto Nacional de Astrofísica, Óptica y Electrónica, Luis E. Erro No. 1, Tonantzintla, 72840 Puebla, Mexico

<sup>16</sup> Space Telescope Science Institute, 3700 San Martin Dr., Baltimore, MD 21218, USA

Received 2021 October 18; revised 2022 February 11; accepted 2022 February 14; published 2022 April 19

## Abstract

We investigate the assembly history of massive disk galaxies and describe how they shape their morphology through cosmic time. Using SHARDS and HST data, we modeled the surface brightness distribution of 91 massive galaxies at redshift  $0.14 < z \leq 1$  in the wavelength range  $0.5\text{--}1.6\ \mu\text{m}$ , deriving the uncontaminated spectral energy distributions of their bulges and disks separately. This spectrophotometric decomposition allows us to compare the stellar population properties of each component in individual galaxies. We find that the majority of massive galaxies ( $\sim 85\%$ ) build inside-out, growing their extended stellar disk around the central spheroid. Some bulges and disks could start forming at similar epochs, but these bulges grow more rapidly than their disks, assembling 80% of their mass in  $\sim 0.7$  and  $\sim 3.5$  Gyr, respectively. Moreover, we infer that both older bulges and older disks are more massive and compact than younger stellar structures. In particular, we find that bulges display a bimodal distribution of mass-weighted ages; i.e., they form in two waves. In contrast, our analysis of the disk components indicates that they form at  $z \sim 1$  for both first- and second-wave bulges. This translates to first-wave bulges taking longer to acquire a stellar disk (5.2 Gyr) compared to second-wave, less compact spheroids (0.7 Gyr). We do not find distinct properties (e.g., mass, star formation timescale, and mass surface density) for the disks in both types of galaxies. We conclude that the bulge mass and compactness mainly regulate the timing of the stellar disk growth, driving the morphological evolution of massive disk galaxies.

*Unified Astronomy Thesaurus concepts:* [Disk galaxies \(391\)](#); [Galaxy classification systems \(582\)](#); [Late-type galaxies \(907\)](#); [Galaxy evolution \(594\)](#); [Galaxy photometry \(611\)](#); [Galaxy spectroscopy \(2171\)](#); [Spectral energy distribution \(2129\)](#); [Galaxy formation \(595\)](#); [Spectrophotometry \(1556\)](#); [Galaxy bulges \(578\)](#); [Galaxy ages \(576\)](#); [Galaxy properties \(615\)](#)

*Supporting material:* machine-readable table

## 1. Introduction

The morphological classification of galaxies represents the first attempt to understand the origins of the variety of observed galaxies in the universe (Hubble 1926). However, a crucial but still unresolved controversy is the origin of the Hubble sequence. When do galaxies shape their morphology? What drives their evolution? How do the spheroidal and disk components of present-day galaxies form?

Traditionally, the stellar disk is proposed to form through the collapse of the gas in a rotating dark matter halo (Fall & Efstathiou 1980). Although the nature of the processes involved is dissipative, the gas conserves its mass and high angular momentum in the absence of external influences (Dalcanton et al. 1997; Mo et al. 1998). Consequently, it enhances a differential star formation in the galaxy, since the central region reaches a sufficient gas surface mass density to form stars earlier or in larger amounts and with higher efficiency than the outer part (Brook et al. 2006). The above description is far from simple within the hierarchical assembly of structures in a cold dark matter universe. Galaxy mergers usually destroy (or thicken) the stellar disk (Steinmetz & Navarro 2002), but the stellar and gas material could survive to



Original content from this work may be used under the terms of the [Creative Commons Attribution 4.0 licence](#). Any further distribution of this work must maintain attribution to the author(s) and the title of the work, journal citation and DOI.

re-form a disk in the merger remnant (Hopkins et al. 2009a; Clauwens et al. 2018).

Multiple possibilities are proposed for the formation of the central bulge component. Accordingly, bulges are usually classified as classical or disklike, depending on their main channel of evolution (Athanasoula 2005). Classical bulges could arise from a violent and dissipative collapse of protogalaxies (Eggen et al. 1962; Larson 1976), accumulation and rearrangement of stars in merger events (Cole et al. 2000; Hopkins et al. 2009b), massive clump coalescence (Noguchi 1999; Bournaud et al. 2007), and/or a gas-compaction phase triggered by violent disk instabilities that lead to efficient spheroidal growth in high-redshift galaxies (Dekel & Burkert 2014; Ceverino et al. 2015; Zolotov et al. 2015). On the other hand, the slow and prolonged rearrangement of disk material due to secular evolutionary processes (i.e., the evolution of a bar component, instabilities due to spiral patterns, etc.) could build up central bulges with disklike properties (Kormendy & Kennicutt 2004; Kormendy 2016). From an observational standpoint, the challenge is to reconstruct the formation pathways of galaxies having access to the observed properties of their bulges and disks (Méndez-Abreu et al. 2010, 2014; Morelli et al. 2015, 2016; Costantin et al. 2017, 2018a, 2018b; de Lorenzo-Cáceres et al. 2019a, 2019b; Gadotti et al. 2020; Gao et al. 2020).

In recent years, there has been a large effort to study the stellar population properties of high-redshift galaxies with the aim of unveiling the main processes that drove their evolution (e.g., Belli et al. 2019; Estrada-Carpenter et al. 2019; Tacchella et al. 2022). These studies suggest that at high redshift, galaxies form on shorter timescales with respect to those formed at later cosmic times. Moreover, the formation redshift of these galaxies seems to depend on their stellar mass (Heavens et al. 2004; Pérez-González et al. 2008; Carnall et al. 2019; Morishita et al. 2019) and mass surface density (Estrada-Carpenter et al. 2020; Suess et al. 2021).

The main problem of studying the galaxy-integrated properties is that the complexity of formation and evolution is averaged out. But until recently, few works have focused their attention on studying the separate evolution of the different morphological components beyond the local universe (e.g., Domínguez-Palmero & Balcells 2008, 2009; Bruce et al. 2014; Margalef-Bentabol et al. 2016; Dimauro et al. 2018; Margalef-Bentabol et al. 2018; Mancini et al. 2019). Thus, in this work, we show how the accreted mass fraction in bulges and disks can actually unveil fundamental hints about the balance between the different pathways of galaxy formation.

In this paper, we study the interplay of bulge and disk properties across time, exploiting the Survey for High- $z$  Absorption Red and Dead Sources (SHARDS; Pérez-González et al. 2013) data set. SHARDS is a state-of-the-art multifilter imaging survey that provides ultradeep ( $m < 26.5$  AB mag) photometry in 25 filters covering the wavelength range 0.50–0.95  $\mu\text{m}$  with subarcsecond seeing. SHARDS data allow us to smoothly sample the spectral energy distribution (SED) of galaxies with spectral resolution  $R \sim 50$  and, given the seeing upper limits imposed in the Gran Telescopio Canarias queue-mode data acquisition, separate the light of their individual bulge and disk components. In Costantin et al. (2021, hereafter Paper I), we presented the spectrophotometric decoupling of a sample of massive galaxies up to redshift  $z = 1$  and their bulge properties. In particular, we found a bimodal distribution of

bulge ages, with a fraction of them being formed in the early universe ( $z \sim 6$ ) and having high mass surface densities; a second wave of bulges, dominant in number, evolved more slowly, forming most of their stars  $\sim 5$  Gyr later. In this second paper of a series, we aim to study the interplay between the bulge and disk properties through time, in order to describe their relative importance in building up massive disk galaxies. For that purpose, we take the same sample presented in Paper I, concentrating on the galaxies with disks (i.e., leaving aside pure spheroids), and study their stellar population properties.

The paper is organized as follows. We describe the data set and summarize the spectrophotometric decoupling procedure and the stellar population analysis in Section 2. We present and discuss our results in Sections 3 and 4, respectively. We provide our conclusions in Section 5. Throughout the paper, we assume a flat cosmology with  $\Omega_m = 0.3$ ,  $\Omega_\Lambda = 0.7$ , a Hubble constant  $H_0 = 70 \text{ km s}^{-1} \text{ Mpc}^{-1}$ , and a Chabrier (2003) initial mass function ( $0.1 < M/M_\odot < 100$ ).

## 2. Data

In this section, we present the data set and the properties of the sample of galaxies analyzed in this work (Section 2.1). The characterization of the bulge and disk physical properties is fully described in Paper I. For completeness, we briefly summarize the main steps of the spectrophotometric decomposition (Section 2.2), as well as the analysis of the stellar population properties (Section 2.3).

### 2.1. Sample of Galaxies

We combine the spectral resolution of the SHARDS observations with the high spatial resolution of the Hubble Space Telescope (HST) Advanced Camera for Surveys and Wide Field Camera 3 (WFC3) images. In particular, we use seven filters for HST images from the optical to the near-infrared wavelength range 0.475–1.600  $\mu\text{m}$  and the 25 filters of SHARDS in the optical wavelength range 0.500–0.941  $\mu\text{m}$  (see Grogin et al. 2011; Koekemoer et al. 2011; Pérez-González et al. 2013; Barro et al. 2019, for details). To provide a more robust constraint on the stellar mass, we complement this data set with the  $K$ -band information at  $\sim 2.1 \mu\text{m}$  provided by the Canada–France–Hawaii Telescope WIRCcam data (Hsu et al. 2019).

In this second paper of a series, we characterize the physical properties of the disk component of massive ( $M_* > 10^{10} M_\odot$ ) and luminous ( $m_{F160W} < 21.5$  mag) galaxies at redshift  $0.14 < z \leq 1$  in the North field of the Great Observatory Origins Deep Survey (GOODS-N). Starting from the parent sample of 478 galaxies defined in Paper I, we consider the 91 galaxies with a reliable photometric bulge+disk decomposition (disky galaxies) and lacking any sign of interactions and/or background/foreground contaminating objects. As discussed in Paper I, the representativeness of the sample in the SHARDS field of view is assured in both redshift and stellar mass by means of a Kolmogorov–Smirnov test ( $p\text{-value}_z > 10\%$ ,  $p\text{-value}_{M_*} > 30\%$ ; see Paper I, for all details about the sample selection).

Our galaxies span a variety of bulge-over-total mass ratios ( $0 \lesssim (B/T)_{\text{mass}} \lesssim 1$ ), bulge mass ( $5 \times 10^8 M_\odot \lesssim M_b \lesssim 2 \times 10^{11} M_\odot$ ), disk mass ( $4 \times 10^8 M_\odot \lesssim M_d \lesssim 10^{11} M_\odot$ ), bulge effective radii ( $0.3 \text{ kpc} \lesssim R_{e,b} \lesssim 5.6 \text{ kpc}$ ), and disk effective radii ( $2.4 \text{ kpc} \lesssim R_{e,d} \lesssim 19 \text{ kpc}$ ). We present in Figure 1 the distribution of

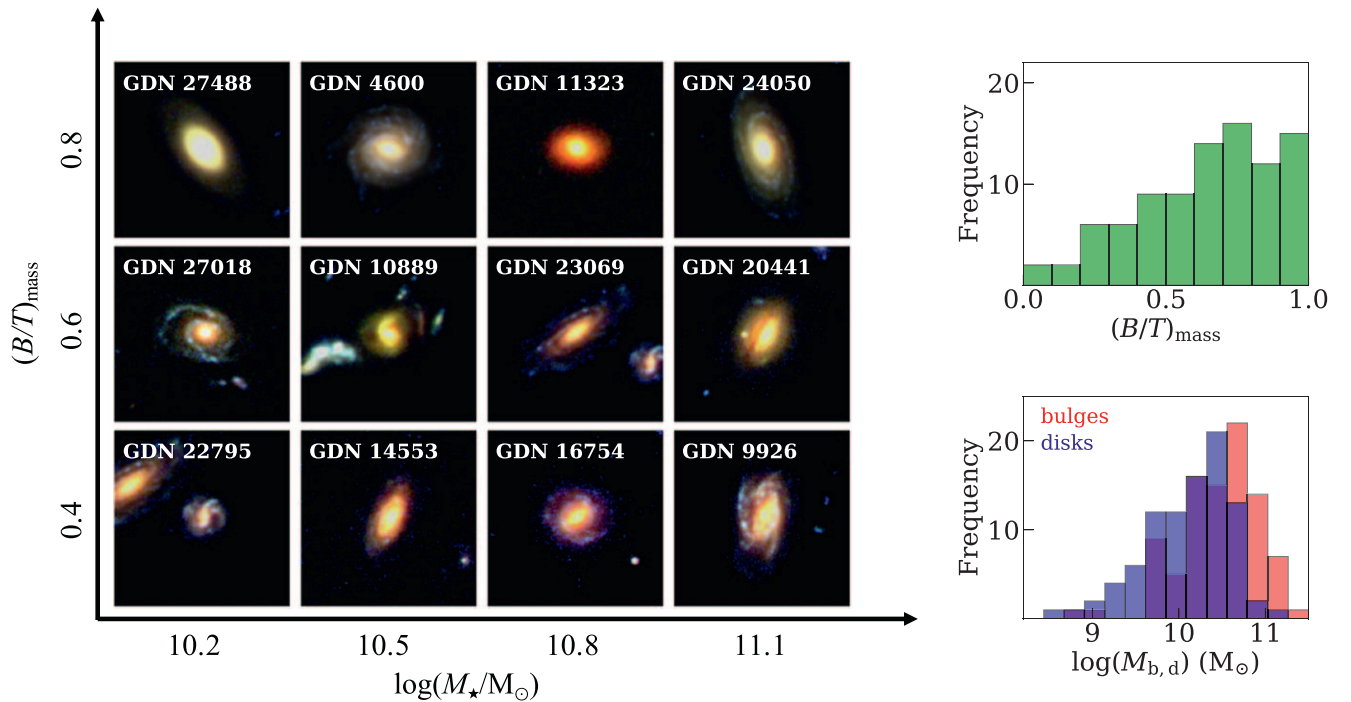


**Figure 1.** Left panel: visual examples from the HST imaging (Koekemoer et al. 2011) of the diversity of morphologies of our galaxies as a function of their stellar mass and bulge-over-total mass ratio  $(B/T)_{\text{mass}}$ . Right panels: bulge-over-total mass ratio (green) and mass distributions of bulges (red) and disks (blue).

$(B/T)_{\text{mass}}$  and stellar mass of the bulge and disk components. Moreover, in Figure 1, we visually demonstrate the large diversity of galaxy morphology as a function of their  $(B/T)_{\text{mass}}$  and galaxy stellar mass.

## 2.2. Spectrophotometric Decomposition

For each galaxy and filter, the bulge and disk light is parameterized to be the sum of a Sérsic (1968) and a single exponential function (Freeman 1970), respectively. We use the GASP2D algorithm (Méndez-Abreu et al. 2008, 2014) to obtain a two-dimensional model of the galaxy across wavelengths. Indeed, we took advantage of the 25 medium-band SHARDS images to spectrophotometrically decouple the different stellar structures with a spectral resolution  $R \sim 50$  in the wavelength range 0.500–0.941  $\mu\text{m}$ . We complement this information with the HST WFC3 and  $K$ -band data, covering the wavelength range between  $\sim 0.5$  and 2  $\mu\text{m}$ . It is worth remembering that the HST photometry is used as a prior for the decoupling of the bulge and disk light in SHARDS images (see Paper I, for details). This strategy mimics the one used by the C2D code (Méndez-Abreu et al. 2019a, 2019b), which allows us to transfer the high spatial resolution of the HST images to the SHARDS data set, consistently reducing the degeneracies associated with the photometric modeling. The procedure eventually provides us with the individual SEDs of each bulge and disk component.

## 2.3. Stellar Populations

We fit both the measured bulge and disk SEDs with the Bruzual & Charlot (2003) stellar population library by means of the `synthesizer` fitting code (see Pérez-González et al. 2003, 2008, for details). Briefly, we assume a Chabrier (2003) initial mass function integrated in the range  $0.1 < M/M_{\odot} < 100$ . The star formation history (SFH) of each

galaxy component is parameterized with a declining delayed exponential law,

$$\text{SFR}(t) \propto t/\tau^2 e^{-t/\tau}, \quad (1)$$

where  $\tau$  runs from 200 Myr to a roughly constant SFH ( $\tau = 100$  Gyr). The metallicity of the models spans discrete values  $Z/Z_{\odot} = [0.4, 1, 2.5]$  (i.e., subsolar, solar, and super-solar). The extinction law of Calzetti et al. (2000) is used to parameterize the  $V$ -band attenuation, with values ranging from 0 to 3 mag.

As described in Paper I, the  $\chi^2$  maximum-likelihood estimator is minimized to obtain the best-fitting model. Moreover, for each galaxy component, we run 500 Monte Carlo simulations to estimate the uncertainties in the stellar population parameters and account for possible degeneracies in the solutions (see Domínguez Sánchez et al. 2016, for more details). As an example, in Figure 2, we present the best model for the bulge, disk, and galaxy SED for the galaxy GDN 10889.

The characterization of each bulge and disk SFH allows us to derive fundamental physical quantities that constrain their stellar populations and is very important in order to quantify their evolutionary process. In particular, in this paper, we will characterize the bulges and disks of the galaxies in our sample in terms of the following physical properties: stellar mass ( $M_{\star}$ ), star formation timescale ( $\tau$ ), metallicity ( $Z$ ), and dust attenuation ( $A_V$ ). Furthermore, we compute the bulge and disk mass-weighted age ( $\bar{t}_M$ ), as well as its corresponding redshift (i.e., the mass-weighted formation redshift  $\bar{z}_M$ ). While mass-weighted ages take into account the extent of the star formation and mitigate the age– $\tau$  degeneracy, the mass-weighted formation redshift allows us to properly compare galaxies observed at different redshift. In order to characterize the beginning and end of the mass assembly of our bulges and disks, we calculate the cosmic times corresponding to the instants when they acquire a fraction of their current mass, starting from the onset

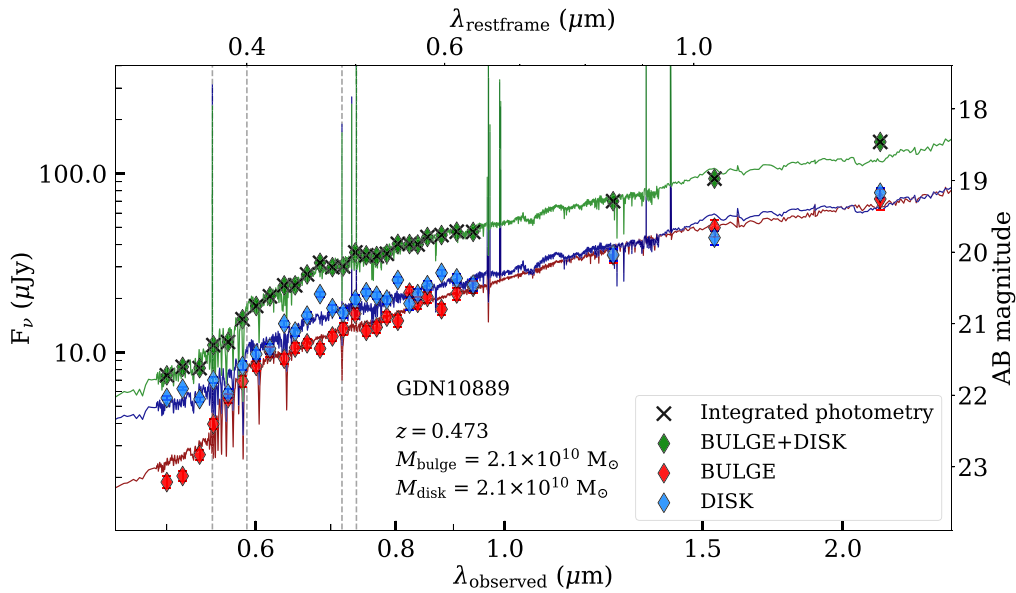


**Figure 2.** The SED of the bulge (red), disk (blue), and galaxy (green) GDN 10889. Diamonds represent the individual photometric results of our decoupling analysis, while black crosses represent the measured integrated photometry of the galaxy in Barro et al. (2019). Errors are reported as 16th–84th percentile intervals. The best models for the bulge, disk, and galaxy are shown as red, blue, and green lines. From left to right, vertical gray dashed lines represent the location of [O II], D4000, H $\beta$ , and [O III] features.

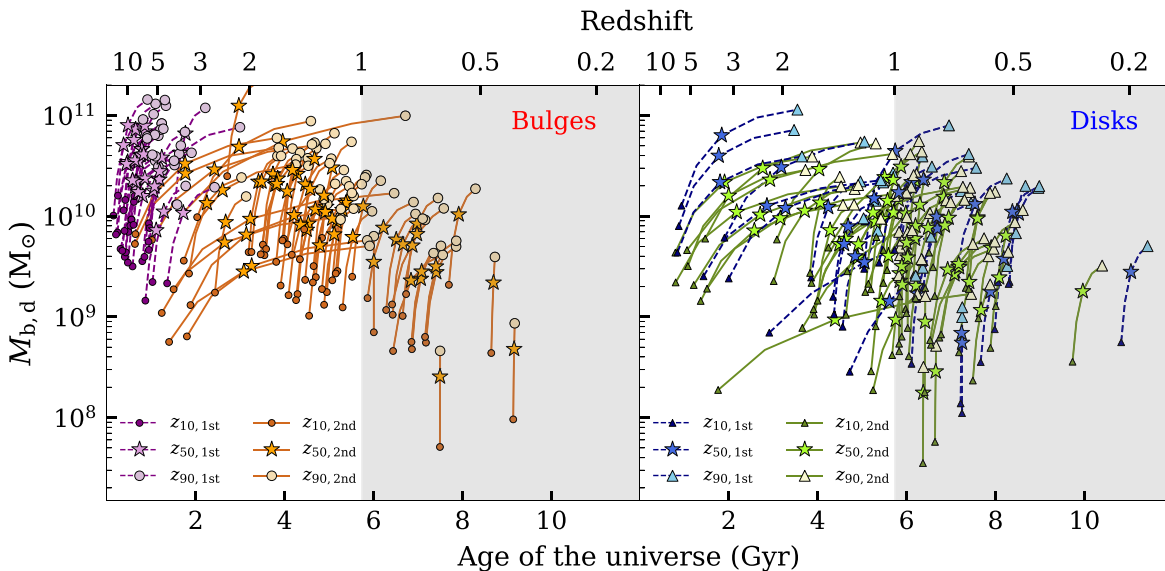


**Figure 3.** Mass assembly history of our bulges (left panel) and disks (right panel) as a function of the age of the universe. Bulges are separated between first-wave (purple dashed lines) and second-wave (orange solid lines) ones. Disks are separated between those around first-wave (blue dashed lines) and second-wave (green solid lines) bulges. For each system, we mark the instants when they build 10%, 50%, and 90% of the current stellar mass (from darker to lighter colors and smaller to larger sizes). In particular, stars stand for  $z_{50}$ , i.e., the redshift when each system grows half of its current mass. The gray shaded regions stand for the redshift of observation.

of the first episode of star formation. In particular, considering their observed redshift, we convert each instant to the corresponding redshift  $z_{10}$ ,  $z_{50}$ , and  $z_{90}$ , i.e., the redshift when each component grows 10%, 50%, and 90% of its current mass (see Figure 3). With this definition,  $z_{50}$  is a proxy for the mass-weighted formation redshift  $\bar{z}_M$ , and they can be compared at first approximation (see Section 3.3). Finally, we also derive the bulge and disk compactness, computing their mass surface density  $\Sigma_{1.5} = MR_e^{-1.5}$  (Barro et al. 2013). We report in Table 1 the properties derived from the main cluster of solutions for the sample galaxies, bulges, and disks.

### 3. Results

In this paper, we focus on the characterization of the stellar disks in a representative sample of massive galaxies at redshift  $0.14 < z \leq 1$ , comparing their properties with those of bulges presented in Paper I. In particular, we present the bulge and disk mass assembly and star formation histories in Sections 3.1 and 3.2, their individual mass-weighted formation redshifts in Section 3.3, and the interplay between their ages and fundamental physical properties (i.e., mass, size, star formation timescale, mass surface density, and Sérsic index) in Section 3.4.

**Table 1**  
Best Parameters for the Sample Galaxies, Bulges, and Disks

ID	$(B/T)_{\text{mass}}$	$R_{e,b}$ (kpc)	$\log(M_b)$ ( $M_\odot$ )	$\bar{t}_{M,b}$ (Gyr)	$\bar{z}_{M,b}$	$\log(\Sigma_{1.5,b})$ ( $M_\odot \text{ kpc}^{-1.5}$ )	$R_{e,d}$ (kpc)	$\log(M_d)$ ( $M_\odot$ )	$\bar{t}_{M,d}$ (Gyr)	$\bar{z}_{M,d}$	$\log(\Sigma_{1.5,d})$ ( $M_\odot \text{ kpc}^{-1.5}$ )
(1)	(2)	(3)	(4)	(5)	(6)	(7)	(8)	(9)	(10)	(11)	(12)
750	$0.85 \pm 0.01$	$1.0 \pm 0.1$	$10.64^{+0.07}_{-0.07}$	$2.5^{+0.3}_{-0.4}$	$1.8^{+0.2}_{-0.2}$	$10.65 \pm 0.07$	$6.7 \pm 0.4$	$9.89^{+0.05}_{-0.05}$	$1.2^{+0.2}_{-0.2}$	$1.27^{+0.06}_{-0.05}$	$8.65 \pm 0.03$
775	$0.55 \pm 0.01$	$0.67 \pm 0.08$	$10.72^{+0.08}_{-0.09}$	$1.4^{+0.1}_{-0.2}$	$1.4^{+0.1}_{-0.1}$	$10.98 \pm 0.08$	$5.7 \pm 0.4$	$10.64^{+0.05}_{-0.05}$	$3.6^{+0.3}_{-0.5}$	$2.9^{+0.5}_{-0.5}$	$9.51 \pm 0.05$
912	$0.72 \pm 0.01$	$0.79 \pm 0.04$	$11.04^{+0.06}_{-0.05}$	$3.7^{+0.4}_{-0.6}$	$1.5^{+0.2}_{-0.2}$	$11.20 \pm 0.03$	$5.3 \pm 0.1$	$10.64^{+0.05}_{-0.05}$	$0.9^{+0.1}_{-0.1}$	$0.75^{+0.03}_{-0.02}$	$9.56 \pm 0.02$
2104	$0.17 \pm 0.01$	$0.36 \pm 0.08$	$10.09^{+0.11}_{-0.09}$	$1.1^{+0.2}_{-0.1}$	$1.0^{+0.1}_{-0.1}$	$10.7 \pm 0.1$	$3.6 \pm 0.1$	$10.78^{+0.07}_{-0.07}$	$3.6^{+0.6}_{-0.7}$	$2.1^{+0.5}_{-0.4}$	$9.94 \pm 0.02$
5131	$0.92 \pm 0.01$	$0.9 \pm 0.2$	$10.60^{+0.07}_{-0.09}$	$5.7^{+0.3}_{-0.7}$	$7.3^{+4.2}_{-3.1}$	$10.7 \pm 0.1$	$2.6 \pm 0.2$	$9.53^{+0.05}_{-0.05}$	$0.16^{+0.03}_{-0.02}$	$0.88^{+0.01}_{-0.01}$	$8.91 \pm 0.04$

**Note.** Table 1 is published in its entirety in machine-readable format. A portion is shown here for guidance regarding its form and content. Column (1): CANDELS ID of the galaxy (Barro et al. 2019). Column (2): mass-weighted  $B/T$ . Column (3): bulge effective radius at  $1.6 \mu\text{m}$  (Paper I). Column (4): bulge stellar mass. Column (5): bulge mass-weighted age. Column (6): bulge mass-weighted formation redshift. Column (7): bulge mass surface density. Column (8): disk effective radius at  $1.6 \mu\text{m}$  (Paper I). Column (9): disk stellar mass. Column (10): disk mass-weighted age. Column (11): disk mass-weighted formation redshift. Column (12): disk mass surface density.

(This table is available in its entirety in machine-readable form.)

### 3.1. Bulge and Disk Mass Assembly History

In this section, we describe how bulges and disks build their mass, focusing on the timescales of their SFHs. This will allow us to understand which component starts to build earlier and at what rate they form.

In Figure 3, we show the stellar masses of our bulges and disks as a function of the age of the universe, i.e., the evolutionary tracks in their stellar mass assembly. We identify (left panel) two behaviors when considering first-wave bulges (those with a mass-weighted formation redshift beyond  $z = 3$ ) and second-wave bulges (those formed from  $z = 3$ ), as identified in Paper I. Indeed, first-wave bulges grow their mass on short timescales,  $t_{90} - t_{10} = 0.68^{+0.05}_{-0.01}$  Gyr; almost identical values are found for those second-wave bulges that start to assemble at redshift  $z \lesssim 2$  ( $t_{90} - t_{10} = 0.68^{+0.03}_{-0.33}$  Gyr). On the other hand, there is a fraction of second-wave bulges (14%) that start to assemble at  $2 \lesssim z \lesssim 5$ , build half of their mass at redshift  $z < 3$ , and evolve more slowly,  $t_{90} - t_{10} = 3.4^{+1.2}_{-1.0}$  Gyr. This subpopulation corresponds to more horizontal evolutionary tracks in the panel.

In Figure 3 (right panel), we see that some disks start to form as early as first-wave bulges ( $z \sim 5$ ). However, they assemble more slowly than bulges ( $t_{90} - t_{10} = 3.5^{+0.9}_{-0.8}$  Gyr), accreting half of their current mass by redshift  $z \sim 2-4$ . This can be understood if a fraction of the primordial gaseous disk forms clumps that migrate to the bulge. In this scenario, only a fraction of the new stars formed in the disk remain in the disk. On the other hand, the evolution of disks that start to form at redshift  $z \lesssim 1.5$  is faster ( $t_{90} - t_{10} = 0.7^{+0.5}_{-0.4}$  Gyr). However, it is worth noticing that 21 out of 66 (32%) of those disks present significant ongoing star formation and/or assembly activity ( $\bar{t}_M < 500$  Myr) at the redshift of observation (see Figure 11). Thus, given that these disks are young, the star formation timescale is not very informative; in principle, they could eventually present similar timescales to those of the disks formed at higher redshift (which we catch in a more evolved evolutionary stage).

We find that the bulk of our disks (76%) grow half of their mass later than bulges, despite some disks having started to form as early as some bulges ( $z \sim 5$ ). Therefore, even if bulges and disks could start forming at the same time, bulges assemble rapidly (short  $\tau_b$ ) and then evolve passively, but disks continue forming stars, so they continue growing more slowly. We note

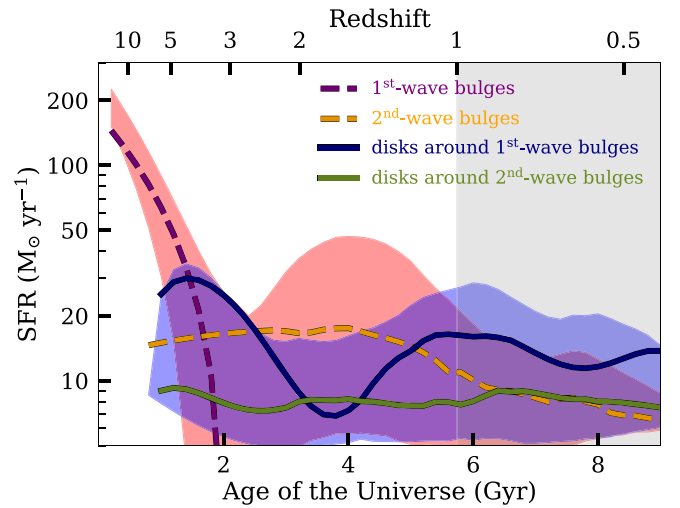


**Figure 4.** Averaged SFHs of the first-wave bulges (purple dashed line) and the disks around them (blue solid line), compared with those of the second-wave bulges (orange dashed line) and the disks around them (green solid line). The red and blue shaded curves represent the 16th–84th percentile interval computed from the scatter of the SFHs of bulges and disks, respectively. The gray shaded area indicates the redshift studied in this work.

that the first-wave bulges present very different timescales compared to the disks around them. The formation of these structures is far enough from the time corresponding to the observed redshift that we can analyze the long-term evolution of bulges and disks. Interestingly, bulges quench quite rapidly, while disks present more extended star formation (see Section 3.2). This indicates that a large amount of gas still exists and falls into the galaxy, but it is not transferred to the central region and/or cannot be transformed efficiently into stars.

### 3.2. Bulge and Disk SFH

As discussed in Paper I, a considerable fraction of our massive galaxies experienced a peak of star formation at  $\bar{z}_{M,b} > 5$  (see Figure 4) linked to a violent episode of compaction (revealed by the high stellar mass densities). The large star formation rate (SFR) values that led to the formation of first-wave bulges are consistent with the high gas accretion rates and the successive compaction events (Zolotov et al. 2015; Ceverino et al. 2018). In particular, Ceverino et al.

(2018) reported typical star formation bursts at  $z = 10$  with a maximum specific SFR of  $\sim 20 \text{ Gyr}^{-1}$ , which translates to  $\text{SFR} \sim 200 M_{\odot} \text{ yr}^{-1}$  for  $10^{10} M_{\odot}$ . This episode causes the rapid growth of a small but massive system, which evolves as a compact spheroid (bulge) and develops an extended (and dynamically stable) stellar disk at later times, as we show in this paper. Thus, we identify these bulges as relics of the blue and red nugget population usually observed at  $z \gtrsim 1.5$  (Damjanov et al. 2009; Barro et al. 2013).

We showed in Figure 3 that the first disks started to form at redshift  $z \sim 5$ . But they build up on longer timescales with respect to bulges, assembling half of their current mass by redshift  $z \sim 2$ . They are characterized by long timescales of evolution ( $\tau_d > 1 \text{ Gyr}$ ), small sizes ( $R_{e,d} \sim 4 \text{ kpc}$ ), and high mass surface densities ( $\log(\Sigma_{1.5,d}) \gtrsim 9.5 M_{\odot} \text{ kpc}^{-1.5}$ ). The compactness of these disks and of first-wave bulges suggests that in the  $z \sim 3$  universe, the conditions were favorable for shaping small and massive systems but with different morphologies.

As shown in Figure 4, the episode of star formation for disks that develop around first-wave bulges is, on average, more intense than the one of disks around second-wave bulges (SFRs of  $\sim 20\text{--}30$  and  $\sim 10 M_{\odot} \text{ yr}^{-1}$ , respectively). As cosmic time passes ( $z \sim 3$  and lower), a second wave of spheroids starts to assemble. These second-wave bulges present a variety of timescales, but the majority of them still form on short timescales ( $\tau_b < 500 \text{ Myr}$ ) with peaks of star formation as intense as  $\sim 50 M_{\odot} \text{ yr}^{-1}$  (and higher than coeval disks). Nevertheless, on average, bulges and disks form stars at similar rates from redshift  $z \sim 1.5$  to 1. At redshift  $z \sim 1$ , our bulges display a drop in star formation, while the disks show a slight increase of star formation activity (until the time of observation).

Summarizing our results in this subsection, we identify four morphological epochs in the evolution of massive disk galaxies. A first wave of bulges started to assemble as early as redshift  $z \sim 10$  ( $\sim 13 \text{ Gyr}$  ago); after some time ( $\sim 12.3 \text{ Gyr}$  ago;  $z \sim 5$ ), the first population (15%) of extended stellar disks started to assemble but on longer timescales than the first wave of bulges. Then, a second wave of bulges, predominant in number (67%), started to grow from redshift  $z \sim 2.5$  down to redshift  $z \sim 1$ . On the top of this second wave, starting from redshift  $z \sim 1.5$  ( $\sim 9.3 \text{ Gyr}$  ago), the disk era starts. Even though bulges are, on average, older than disks (see Section 3.3.2), we find a close interplay between the two components, which suggests a level of coevolution between them. This will be further discussed in Section 4.

### 3.3. Mass-weighted Formation Redshifts

We derive the mass-weighted ages of each bulge and disk, providing fundamental constraints on their formation and coevolution (see Table 1 and Appendix). Our galaxies are observed in a wide redshift range,  $0.14 < z \leq 1$  (spanning  $\sim 6 \text{ Gyr}$  of cosmic time), making the interpretation of their mass-weighted ages more difficult. Thus, we compute the redshift corresponding to their mass-weighted ages ( $\bar{z}_M$ ; see Table 1) to follow the evolution of each system at different epochs. In Figure 5, we show the mass-weighted formation redshift of bulges and disks as a function of their stellar mass. As already discussed in Section 3.1, we find that the disk population forms, on average, at later cosmic times than the bulge population. Bulges have a median mass-weighted

formation redshift  $\bar{z}_{M,b} = 1.6^{+4.6}_{-0.7}$ , while disks have  $\bar{z}_{M,d} = 1.0^{+0.6}_{-0.3}$ . In Paper I, we found that 33% of bulges have  $\bar{z}_{M,b} > 3$ . Here we show that only 10 out of 91 disks have  $\bar{z}_{M,d} > 2$ , and none of them present  $\bar{z}_{M,d} > 3.2$ . These findings are consistent with the predictions from multiple cosmological simulations, where the spheroidal component tends to form at early cosmic epochs, and late star formation contributes to the growth of disk stars. In particular, Park et al. (2019) quantified that massive galaxies ( $10 < \log(M_{z=0.7}/M_{\odot}) < 11$ ) in the New Horizon simulations (Dubois et al. 2021) start to form disks from  $z \sim 1\text{--}2$ , once their mass becomes  $\sim 10^{10} M_{\odot}$ . Tacchella et al. (2019) showed that the efficiency of disk formation in IllustrisTNG simulations (Nelson et al. 2018; Pillepich et al. 2018) strongly depends on both stellar mass and cosmic time. In both simulations, at early times, the formation efficiency of disks is low, increasing toward  $z \sim 1$ .

Bulges formed at higher redshift are more massive (Paper I), as proved by a Spearman correlation coefficient of 0.71 ( $p$ -value  $< 0.01$ ). Similarly, older disks are more massive (Spearman correlation coefficient of 0.40;  $p$ -value  $< 0.01$ ). On the other hand, the bulge formation time has a stronger correlation with the total mass of the galaxy than disks, having a Spearman correlation coefficient of 0.63 and 0.36, respectively. These trends are in agreement with the fact that there is a strong correlation between mass and cosmic time, as shown in both the FIRE (Hopkins et al. 2014) and the New Horizon cosmological simulations. In particular, massive galaxies start to form disk stars at earlier epochs ( $z \gtrsim 1$ ), while low-mass galaxies develop their disks after  $z \sim 1$  (El-Badry et al. 2018; Park et al. 2019).

#### 3.3.1. First- and Second-wave Systems

As discussed in Paper I, bulges form in two waves. The distribution of their mass-weighted formation redshift is bimodal: first-wave bulges have a median mass-weighted formation redshift  $\bar{z}_{M,b} = 6.2^{+1.5}_{-1.7}$ , while second-wave bulges have  $\bar{z}_{M,b} = 1.3^{+0.6}_{-0.6}$ . Our analysis allows us to directly compare the disks that build up around first-wave bulges with the ones growing around second-wave bulges. The first ones have a median mass-weighted formation redshift  $\bar{z}_{M,d} = 0.9^{+0.9}_{-0.4}$ , while the latter ones have  $\bar{z}_{M,d} = 1.0^{+0.6}_{-0.3}$ . A Kolmogorov–Smirnov test ( $K = 0.15$ ,  $p$ -value  $> 0.6$ ) suggests that we cannot reject the null hypothesis that the two  $\bar{z}_{M,d}$  distributions are identical. Thus, at the peak of the cosmic SFR density (Lilly et al. 1996; Madau et al. 1996; Madau & Dickinson 2014), disks could form around all types of spheroids.

We find that most of our disks formed at similar cosmic times as second-wave bulges ( $\bar{z}_M \sim 1$ ). Nonetheless, the disk’s  $\bar{z}_{M,d}$  (and  $\bar{t}_{M,d}$ ) distribution is different from the one of second-wave bulges at a  $3\sigma$  confidence level, as proved by a Kolmogorov–Smirnov test with statistic  $K = 0.35$  ( $K = 0.30$ ).

#### 3.3.2. Age Difference between Bulges and Disks

In order to characterize the galaxy evolution in terms of its structural components, we show in Figure 6 the differences in mass-weighted ages between each bulge and disk. The median age difference is  $\Delta \bar{t}_{M,bd} = \bar{t}_{M,b} - \bar{t}_{M,d} = 1.6^{+5.4}_{-0.7} \text{ Gyr}$ .

We define bulges as older, coeval, and younger than their disks by looking at the compatibility between each  $\Delta \bar{t}_{M,bd} \pm \sigma_{\Delta \bar{t}_{M,bd}}$  and  $\Delta \bar{t}_{M,bd} = 0$ . At the  $1\sigma$  ( $3\sigma$ ) level we

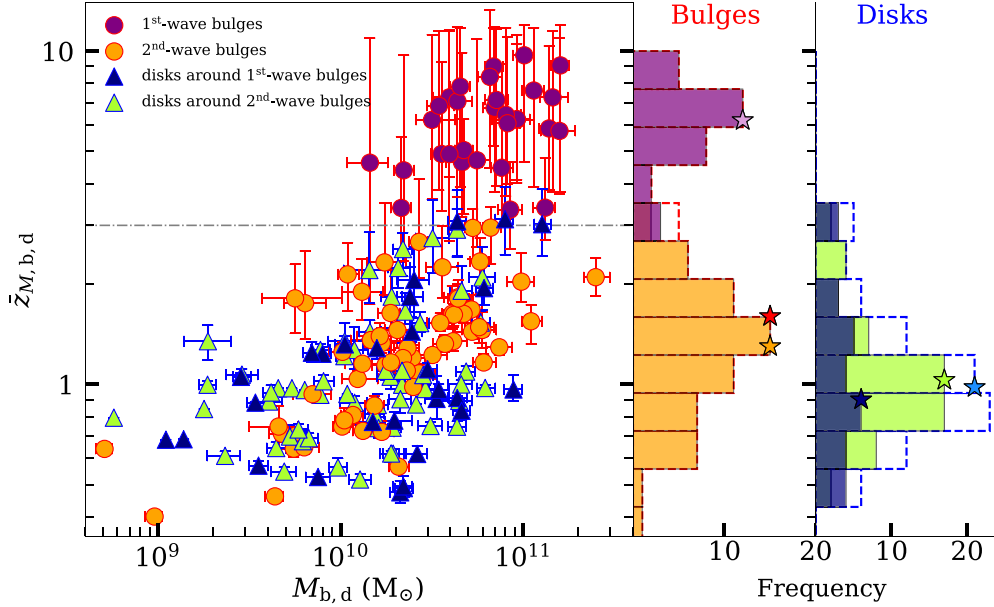


**Figure 5.** Mass-weighted formation redshift of bulges (dots) and disks (triangles) as a function of their stellar mass. Bulges and disks are separated into first-wave (purple and blue, respectively) and second-wave (orange and green, respectively) ones. Errors are reported as a 16th–84th percentile interval. The gray dashed–dotted horizontal line marks  $z_M = 3$ . The histograms represent the frequency of the mass-weighted formation redshifts of the bulge and disk populations. Purple and orange histograms stand for first- and second-wave bulges, while the red dashed histogram stands for the entire bulge population. Blue and green histograms stand for disks around first- and second-wave bulges, while the blue dashed histogram stands for the entire disk population. The median values of each distribution are marked with stars.

find that 74% (59%) of our bulges formed before their disks, 9% (29%) of systems are compatible to being coeval, while in 17% (12%) of galaxies, the bulge formed after the disk component. In particular, all first-wave bulges are older than their disk component. We find that first-wave bulges and their disks present  $\Delta\bar{t}_{M,bd} = 5.2^{+1.1}_{-1.9}$  Gyr, while the age difference for second-wave systems is  $\Delta\bar{t}_{M,bd} = 0.7^{+1.5}_{-1.6}$  Gyr. In the following, we analyze the properties of bulges and disks considering the age difference between the two components at the  $1\sigma$  level.

As discussed in Section 4, our results actually suggest that (second-wave) bulges and disks display a degree of coevolution; both structures form at similar times ( $z_{10}$ ), but the disk builds up on longer timescales, continuing to form stars, while the bulge stops its star formation earlier (see Figures 3 and 4).

### 3.4. Morphological Properties

In this section, we analyze the physical properties regulating the bulge and disk evolution. In particular, we focus on their stellar mass, size, timescale, mass surface density, and Sérsic index.

#### 3.4.1. Stellar Mass

Our bulges have a median  $\log(M_b/M_\odot) = 10.5^{+0.3}_{-0.5}$ , while our disks have a median  $\log(M_d/M_\odot) = 10.2^{+0.4}_{-0.6}$ .

We find that first- and second-wave bulges have a median  $\log(M_b/M_\odot) = 10.8^{+0.2}_{-0.3}$  and  $10.3^{+0.4}_{-0.5}$ , respectively. On the other hand, disks around first- and second-wave bulges have similar masses of  $\log(M_d/M_\odot) = 10.3^{+0.3}_{-0.7}$  and  $10.2^{+0.3}_{-0.5}$ , respectively. A Kolmogorov–Smirnov test suggests that we cannot reject the null hypothesis that both the two  $M_d$  distributions ( $K = 0.27$ ,  $p$ -value  $> 0.08$ ) and the distributions

of  $M_d$  and  $M_b$  for second-wave bulges ( $K = 0.17$ ,  $p$ -value  $> 0.2$ ) are similar.

In terms of their mass, bulges older, coeval, and younger than their disks have a median mass  $\log(M_b/M_\odot) = 10.6^{+0.3}_{-0.5}$ ,  $10.4^{+0.1}_{-0.2}$ , and  $10.1^{+0.2}_{-0.5}$ , respectively. There is a (mild) correlation (Spearman coefficient of 0.48;  $p$ -value  $< 0.01$ ) between  $\Delta\bar{t}_{M,bd}$  and  $M_b$ . In particular, in the high-mass regime ( $M_b > 3 \times 10^{10} M_\odot$ ), there is only one bulge (out of 54) younger than its disk (see Figure 6). Disks younger, coeval, and older than their bulges have median a mass  $\log(M_d/M_\odot) = 10.2^{+0.3}_{-0.6}$ ,  $10.4^{+0.3}_{-0.6}$ , and  $10.3^{+0.3}_{-0.2}$ , respectively. There is no correlation between  $\Delta\bar{t}_{M,bd}$  and  $M_d$ .

We now investigate the relative contribution of bulges and disks to the total stellar mass of our galaxies. The median bulge-over-total mass ratio of the sample is  $(B/T)_{\text{mass}} = 0.69^{+0.21}_{-0.31}$ . Galaxies that build from first-wave systems are more bulge-dominated than those that build later on, having  $(B/T)_{\text{mass}} = 0.76^{+0.16}_{-0.18}$  and  $0.63^{+0.22}_{-0.29}$ , respectively. There is a mild correlation between the bulge prominence and its formation redshift (Spearman coefficient of 0.45;  $p$ -value  $< 0.01$ ), while we find no correlation between the disk  $z_{M,d}$  and  $(B/T)_{\text{mass}}$ .

We find a trend between  $\Delta\bar{t}_{M,bd}$  and the prominence of the two components defined by  $(B/T)_{\text{mass}}$ , as shown in Figure 6. The Spearman correlation coefficient of  $(\Delta\bar{t}_{M,bd}, (B/T)_{\text{mass}})$  is 0.49 ( $p$ -value  $< 0.01$ ). We find that 48% of bulges in galaxies with  $B/T < 0.5$  are younger than their disks (12 out of 25), while this fraction diminishes to 6% for bulges in galaxies with  $B/T > 0.5$ . In particular, bulges older than their disks reside in galaxies with a median  $(B/T)_{\text{mass}} = 0.75^{+0.16}_{-0.20}$ , bulges with ages similar to those of their disks reside in galaxies with a median  $(B/T)_{\text{mass}} = 0.46^{+0.23}_{-0.11}$ , and bulges younger than their disks are found in galaxies with a median  $(B/T)_{\text{mass}} = 0.34^{+0.18}_{-0.16}$ .

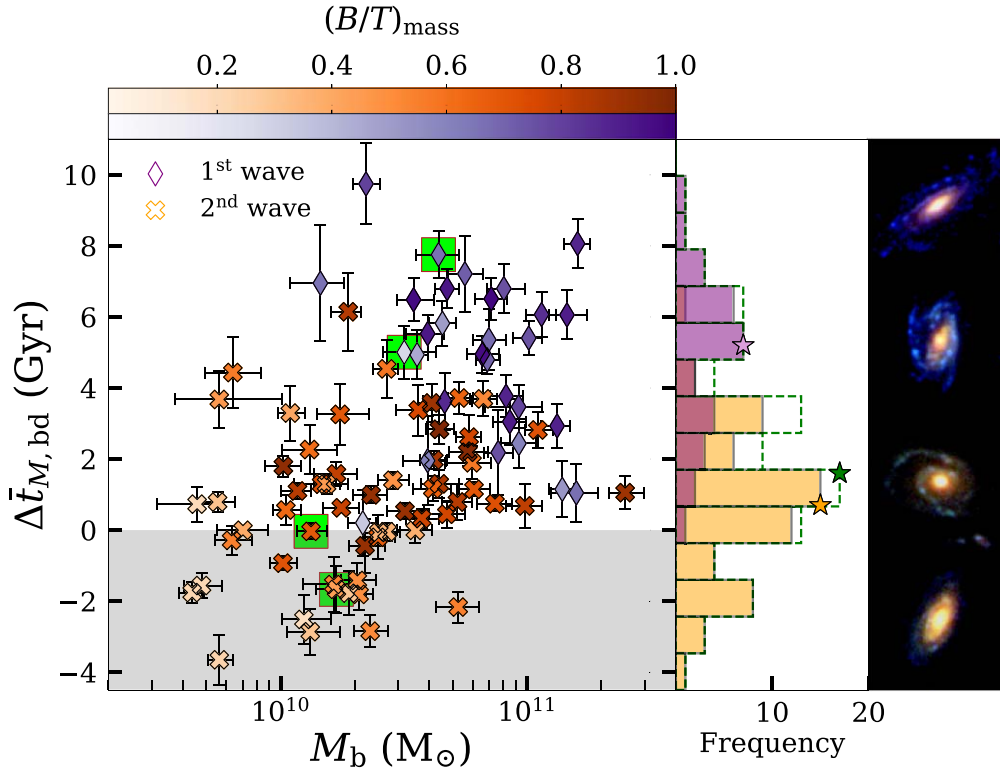


**Figure 6.** Age difference between each bulge and disk as a function of the bulge mass, color-coded according to  $(B/T)_{\text{mass}}$ . Errors are reported as the 16th–84th percentile interval. The gray shaded region marks  $\Delta\bar{t}_{M,\text{bd}} < 0$ . Green squares mark the four galaxies shown in RGB colors as an example (right panels). The purple histogram stands for galaxies with first-wave bulges, the orange histogram stands for galaxies with second-wave bulges, and the green dashed histogram stands for the entire population. The median values of each distribution are marked with stars.

### 3.4.2. Size

We define the size by means of the effective radius  $R_e$ , i.e., the radius at which bulges and disks contain half of their light in the WFC3 F160W band. In particular, being the surface brightness of the disk modeled with an exponential profile with scale radius  $h$  (Paper I), the effective radius corresponds to  $R_{e,d} = 1.678 \times h$  (Graham & Driver 2005).

Bulges and disks have median sizes  $R_{e,b} = 1.0^{+0.9}_{-0.4}$  and  $R_{e,d} = 5.4^{+3.4}_{-2.0}$  kpc, respectively. We find that first- and second-wave bulges have similar median sizes, i.e.,  $R_{e,b} = 1.3^{+0.8}_{-0.6}$  and  $1.0^{+0.8}_{-0.4}$  kpc, respectively. On the other hand, we show in Figure 7 that disks around first- and second-wave bulges have  $R_{e,d} = 6.3^{+3.1}_{-2.5}$  and  $4.8^{+2.8}_{-1.4}$  kpc, respectively. Disks around first-wave bulges are larger than those around second-wave bulges at a  $2\sigma$  confidence level ( $K = 0.31$ ). In Paper I, we found a weak correlation (Spearman coefficient of 0.21) between the mass-weighted formation redshift of bulges and their size. However, there is no correlation between the disk size and the time of their formation (Figure 7). This remains valid if we separate disks into those around first- and second-wave bulges.

In terms of their size, bulges older, coeval, and younger than their disks have median sizes  $R_{e,b} = 1.1^{+0.9}_{-0.4}$ ,  $1.0^{+0.4}_{-0.2}$ , and  $0.7^{+0.7}_{-0.3}$  kpc, respectively. Disks younger, coeval, and older than their bulges have median sizes  $R_{e,d} = 6.0^{+3.1}_{-2.4}$ ,  $6.9^{+0.5}_{-3.4}$ , and  $3.6^{+1.9}_{-0.6}$  kpc, respectively. There is no correlation between either  $\Delta\bar{t}_{M,\text{bd}}$  and  $R_{e,b}$  or  $\Delta\bar{t}_{M,\text{bd}}$  and  $R_{e,d}$ .

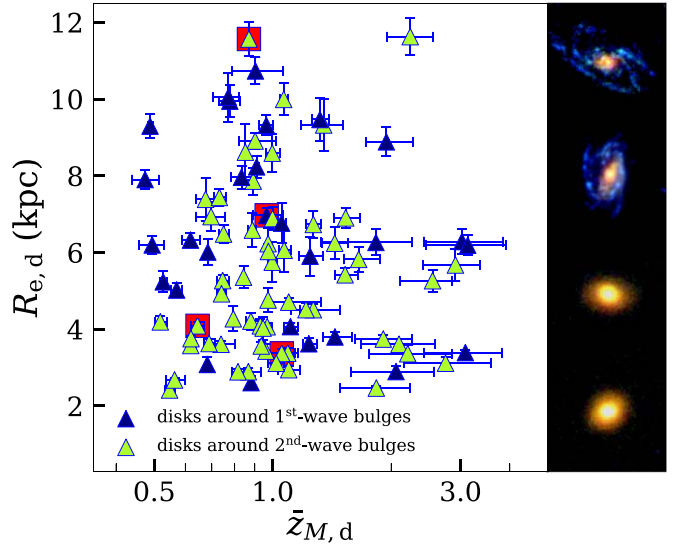


**Figure 7.** Size of disks as a function of their mass-weighted formation redshift. Disks around first- and second-wave bulges are shown in blue and green, respectively. Errors are reported as the 16th–84th percentile interval. Red squares mark the four galaxies shown in RGB colors as an example (right panel).

### 3.4.3. Star Formation Timescale

The disks of our massive galaxies present a median  $\tau_d = 320^{+950}_{-110}$  Myr. As highlighted in Paper I, bulges mostly formed on short timescales ( $\tau \sim 200$  Myr), and a slower mode of formation starts to be in place only for some second-wave bulges. On the other hand, we find that 52% of disks have

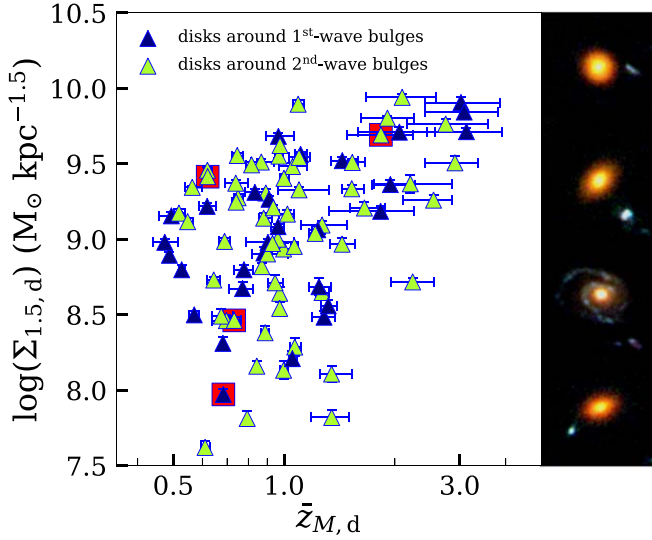


**Figure 8.** Mass surface density of disks as a function of their mass-weighted formation redshift. Disks around first- and second-wave bulges are shown in blue and green, respectively. Errors are reported as the 16th–84th percentile interval. Red squares mark the four galaxies shown in RGB colors as an example (right panel).

$\tau_d > 300$  Myr and 38% of disks have  $\tau_d > 500$  Myr. The first disks in place ( $z_{M,d} \sim 2$ –3) formed on longer timescales compared to the ones formed at lower redshift. Indeed, all disks formed at redshift  $z_{M,d} > 1.7$  have  $\tau_d \gtrsim 800$  Myr.

Disks around first- and second-wave bulges have a median  $\tau_d = 360_{-160}^{+610}$  and  $320_{-110}^{+1110}$  Myr, respectively. A Kolmogorov–Smirnov test ( $K = 0.11$ ,  $p$ -value  $> 0.9$ ) suggests that we cannot reject the null hypothesis that these two distributions are similar.

We find that disks older than their bulges form on longer timescales compared with the younger ones. Indeed, disks younger and older than bulges have  $\tau_d = 260_{-60}^{+680}$  and  $900_{-690}^{+550}$  Myr, respectively.

#### 3.4.4. Mass Surface Density

We parameterize the bulge and disk compactness by looking at their mass surface density  $\Sigma_{1.5}$  (see Section 2.3). As expected, we find that bulges and disks have very different mass surface densities; bulges present a median  $\log(\Sigma_{1.5,b}) = 10.4_{-0.6}^{+0.5} M_\odot \text{kpc}^{-1.5}$ , while disks have a median  $\log(\Sigma_{1.5,d}) = 9.1_{-0.6}^{+0.4} M_\odot \text{kpc}^{-1.5}$ .

We show the trend between  $z_{M,d}$  and  $\log(\Sigma_{1.5,d})$  in Figure 8. There is a mild trend between the disk mass-weighted formation redshift and the mass surface density (Spearman coefficient of 0.36;  $p$ -value  $< 0.01$ ); i.e., older disks are more compact.

We already discussed in Paper I that first-wave bulges display higher values of mass surface density than second-wave bulges; i.e., they are more compact ( $\log(\Sigma_{1.5,b}) = 10.6_{-0.4}^{+0.4}$  and  $10.2_{-0.4}^{+0.5} M_\odot \text{kpc}^{-1.5}$ , respectively). This is a hint for characterizing their different formation mechanisms. But we find no differences of  $\Sigma_{1.5,d}$  between disks around first- and second-wave bulges ( $\log(\Sigma_{1.5,d}) = 9.0_{-0.5}^{+0.6}$  and  $9.1_{-0.7}^{+0.4} M_\odot \text{kpc}^{-1.5}$ , respectively). Nonetheless, we find that the first structures to form are the more compact. This is valid not only for galaxies but also for each of their morphological components.

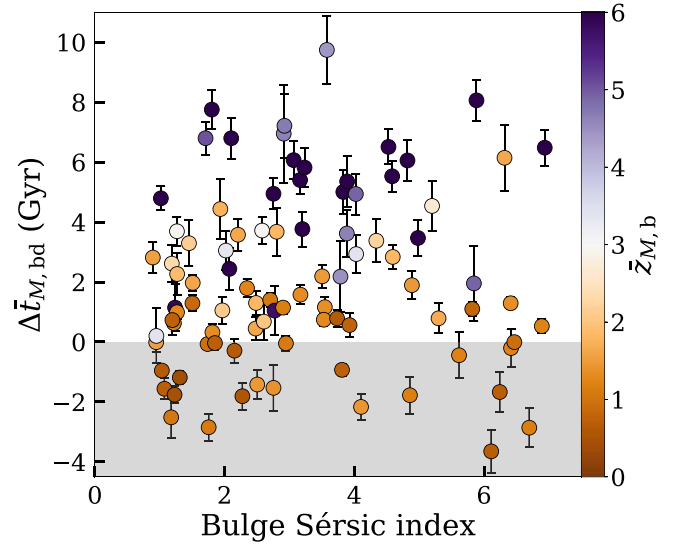


**Figure 9.** Age difference of bulges and disks as a function of the bulge Sérsic index, color-coded according to the bulge mass-weighted formation redshift. Errors are reported as the 16th–84th percentile interval. The gray shaded region marks  $\Delta t_{M,bd} < 0$ .

#### 3.4.5. Sérsic Index

We find that neither the mass-weighted formation redshift of bulges nor that of disks correlates with the bulge Sérsic index, having Spearman coefficients of 0.12 and  $-0.01$ , respectively ( $p$ -value  $> 0.25$  and  $0.90$ , respectively). Moreover, bulge and disk mass-weighted formation redshifts do not correlate with the Sérsic index of the galaxy either, having Spearman coefficients of 0.15 and 0.17, respectively ( $p$ -value  $> 0.15$  and  $0.11$ , respectively). As shown in Figure 9, no correlation is found between the  $\Delta t_{M,bd}$  and the bulge Sérsic index, being the Spearman coefficient of  $\sim 0.13$  ( $p$ -value  $> 0.21$ ).

## 4. Discussion

In this section, we discuss the main results of our analysis, summarizing our findings about bulge and disk formation (presented in Paper I and this paper). To facilitate the comparison, we briefly outline all of the physical properties measured for our bulges and disks (in Table 2), dividing the systems between first- and second-wave, as well as separating galaxies into those with bulges older, coeval, or younger than their disks. Moreover, we qualitatively illustrate in Figure 10 the proposed scenario for the formation and morphological evolution of massive disk galaxies at redshift  $0.14 < z \leq 1$ , complementing the picture provided in Paper I (Figure 13) and adding the information about the disk epoch.

Galaxies are complex systems, and their integrated properties are hiding the complexity of their evolution. Indeed, we infer from our results that we are looking at an evolutionary sequence in which massive disk galaxies shape their morphology, growing their extended stellar disks around a centrally concentrated spheroid. The residual and continuous gas accretion enables the central spheroid to slowly develop a stellar envelope, allowing the incoming gas to retain angular momentum and resulting in a more extended and disk system by  $z \lesssim 1$  (see also Pérez-González et al. 2008; Buitrago et al. 2013). In particular, we find that disks form efficiently when bulges grow inefficiently, and vice versa (Figures 4 and 5). Indeed, we report a delay in the time of formation of the two

**Table 2**  
Median Physical Properties of Bulges and Disks at Redshift  $0.14 < z \leq 1$

Type	$\log(M_*)$ ( $M_\odot$ )	$\bar{t}_M$ (Gyr)	$\bar{z}_M$	$z_{10}$	$z_{90}$	$\tau$ (Myr)	$R_e$ (kpc)	$\log(\Sigma_{1.5})$ ( $M_\odot \text{ kpc}^{-1.5}$ )
(1)	(2)	(3)	(4)	(5)	(6)	(7)	(8)	(9)
Bulges	$10.5^{+0.3}_{-0.5}$	$2.7^{+3.9}_{-1.6}$	$1.6^{+4.6}_{-0.7}$	$2.0^{+6.8}_{-1.0}$	$1.3^{+3.4}_{-0.6}$	$210^{+480}_{-10}$	$1.0^{+0.9}_{-0.4}$	$10.4^{+0.5}_{-0.6}$
First-wave bulges	$10.8^{+0.2}_{-0.3}$	$6.5^{+1.5}_{-1.4}$	$6.2^{+1.5}_{-1.7}$	$8.8^{+3.9}_{-2.9}$	$4.7^{+0.7}_{-1.2}$	$200^{+20}_{-10}$	$1.3^{+0.8}_{-0.6}$	$10.6^{+0.4}_{-0.4}$
Second-wave bulges	$10.3^{+0.4}_{-0.5}$	$1.7^{+2.0}_{-0.8}$	$1.3^{+0.6}_{-0.6}$	$1.4^{+1.9}_{-0.6}$	$1.1^{+0.4}_{-0.4}$	$210^{+790}_{-10}$	$1.0^{+0.8}_{-0.4}$	$10.2^{+0.5}_{-0.4}$
Bulges older than disks	$10.6^{+0.3}_{-0.5}$	$4.5^{+2.7}_{-2.8}$	$2.3^{+4.5}_{-1.0}$	$4.0^{+6.2}_{-2.6}$	$1.7^{+3.3}_{-0.6}$	$210^{+480}_{-10}$	$1.1^{+0.9}_{-0.4}$	$10.5^{+0.5}_{-0.6}$
Bulges coeval with disks	$10.4^{+0.1}_{-0.2}$	$1.4^{+1.9}_{-0.6}$	$1.1^{+0.4}_{-0.4}$	$1.2^{+0.4}_{-0.4}$	$1.0^{+0.3}_{-0.4}$	$230^{+80}_{-20}$	$1.0^{+0.4}_{-0.2}$	$10.3^{+0.3}_{-0.4}$
Bulges younger than disks	$10.1^{+0.2}_{-0.5}$	$1.1^{+0.4}_{-1.0}$	$0.8^{+0.5}_{-0.2}$	$0.9^{+0.6}_{-0.2}$	$0.8^{+0.4}_{-0.3}$	$200^{+510}_{-10}$	$0.7^{+0.7}_{-0.3}$	$10.1^{+0.5}_{-0.3}$
Disks	$10.2^{+0.4}_{-0.6}$	$1.2^{+1.6}_{-0.9}$	$1.0^{+0.6}_{-0.3}$	$1.0^{+1.7}_{-0.4}$	$0.9^{+0.3}_{-0.3}$	$320^{+950}_{-110}$	$5.4^{+3.4}_{-2.0}$	$9.1^{+0.4}_{-0.6}$
Disks around first-wave bulges	$10.3^{+0.3}_{-0.7}$	$1.3^{+1.8}_{-0.9}$	$0.9^{+0.9}_{-0.4}$	$1.1^{+2.1}_{-0.5}$	$0.8^{+0.4}_{-0.3}$	$360^{+610}_{-160}$	$6.3^{+3.1}_{-2.5}$	$9.0^{+0.6}_{-0.5}$
Disks around second-wave bulges	$10.2^{+0.3}_{-0.5}$	$1.0^{+1.7}_{-0.8}$	$1.0^{+0.6}_{-0.3}$	$1.0^{+1.1}_{-0.2}$	$0.9^{+0.2}_{-0.3}$	$320^{+1110}_{-110}$	$4.8^{+2.8}_{-1.4}$	$9.1^{+0.4}_{-0.7}$
Disks younger than bulges	$10.2^{+0.3}_{-0.6}$	$0.8^{+0.9}_{-0.6}$	$0.9^{+0.4}_{-0.3}$	$1.0^{+0.6}_{-0.3}$	$0.9^{+0.2}_{-0.3}$	$260^{+680}_{-60}$	$6.0^{+3.1}_{-2.4}$	$9.0^{+0.5}_{-0.5}$
Disks coeval with bulges	$10.4^{+0.3}_{-0.6}$	$1.6^{+2.1}_{-0.7}$	$1.2^{+0.3}_{-0.4}$	$1.6^{+1.8}_{-0.7}$	$0.9^{+0.2}_{-0.2}$	$750^{+2140}_{-340}$	$6.9^{+0.5}_{-3.4}$	$9.2^{+0.6}_{-0.8}$
Disks older than bulges	$10.3^{+0.3}_{-0.2}$	$2.9^{+0.9}_{-1.7}$	$1.5^{+1.0}_{-0.6}$	$2.8^{+2.5}_{-1.9}$	$0.9^{+0.4}_{-0.3}$	$900^{+550}_{-690}$	$3.6^{+1.9}_{-0.6}$	$9.4^{+0.4}_{-0.3}$

**Note.** Column (1): morphological component. Column (2): stellar mass. Column (3): mass-weighted age. Column (4): mass-weighted formation redshift. Column (5): redshift when a component grows 10% of its current mass. Column (6): redshift when a component grows 90% of its current mass. Column (7): timescale of exponentially declined SFH. Column (8): effective radius. Column (9): mass surface density.

components. This is consistent with recent cosmological simulations (e.g., IllustrisTNG) showing that bulges form efficiently at early cosmic times and assemble most of their mass by the time galaxies stop forming stars (Tacchella et al. 2019).

Our main result is that disks consistently form at  $z \sim 1$  around first- and second-wave bulges. This evidence may suggest that disks at these redshifts are not destroyed, while they might be at higher redshift ( $z \gtrsim 3-5$ ). The reasons for this might be the enhanced merger activities and the (larger) more turbulent gas fractions. Thus, primordial (dynamically unstable) gas-rich disks have a different fate than extended thin (dynamically stable) disks, which grow at  $z \lesssim 1$ . Furthermore, first- and second-wave bulges also show very different paths of evolution, the former being products of compaction events at very high redshift (Paper I).

In the two-phase scenario proposed for early-type galaxies (Oser et al. 2010), a compact progenitor rapidly built at high redshift (Dekel et al. 2009; Zolotov et al. 2015; Flores-Freitas et al. 2022) and slowly grew in size through nondissipational processes (e.g., dry minor mergers) until resulting in an elliptical galaxy in the local universe (Naab et al. 2009; Huang et al. 2013a, 2013b). In this picture, we argue that massive disk galaxies could also play a crucial role, hosting a compact core (first-wave bulge) that went through a blue and red nugget phase and grew an extended stellar disk at later times. Moreover, some of the second-wave bulges are as compact as first-wave bulges and formed before their disks. They could be interpreted as a later wave of systems going through a red nugget phase at  $z < 3$  but keeping in mind that these galaxies experienced a higher degree of coevolution between the spheroidal and disk component (see Section 3.3.2). This could allow one to extend the two-phase paradigm to late-type galaxies, as already proposed by recent studies (Graham 2013; de la Rosa et al. 2016; Costantin et al. 2020).

We remark that only a proper decoupling of the two components allows us to characterize the instants where these galaxies form and the physical processes responsible for their evolution. In this picture, the results of our work point toward a scenario where the majority of massive disk galaxies assemble

inside-out. In  $\sim 75\%$  of our galaxies, the central bulge forms half of its mass earlier than the disk component, which takes, on average,  $\sim 1.5$  Gyr to develop around the bulge. In particular, for  $\sim 35\%$  of the systems, the bulge takes more than 3 Gyr to develop an extended disk. This result is consistent with predictions from EAGLE cosmological simulations (Crain et al. 2015; Schaye et al. 2015) showing that on average, disk-dominated galaxies more massive than  $10^{10} M_\odot$  have inner regions older than the outer part ( $\sim 1$  Gyr at  $z = 0.5$ ), compatible with an inside-out formation (Pfeffer et al. 2022).

The few disks (17%) older than their bulges are characterized by longer timescales with respect to disks younger than their bulges. Considering that some disks start to form as early as some bulges, but they assemble their mass slower, this suggests a high degree of coevolution between the two components. Disk material is probably accreted into the central region of the galaxy, funneling gas and highly increasing the star formation efficiency of the spheroidal component. However, since bulges build up fast, as time passes, we see residual star formation in the disk component simultaneously with a reduction of the star formation activity in the central region of the galaxy.

Focusing on the first-assembled systems ( $z \sim 10$ ), we find that they grow an extended stellar disk from a spheroidal-like system (first-wave bulge). In this scenario, cosmological simulations show that it is possible to form extended star-forming disks around red nuggets after compaction (Zolotov et al. 2015; Dekel et al. 2020). Given that first-wave bulges are very massive and compact, and considering the mass-weighted age differences between the bulge and the disk in these galaxies, our results point to a morphological quenching and a stabilization of the galaxies that prevents further star formation in the primordial disk for several gigayears. In these galaxies, it is possible that the compaction phase of first-wave bulges consumes the cold gas in the outskirts (or quickly destroys the primordial disk) and inhibits the star formation for as long as  $\sim 8$  Gyr (see Figure 6). Even if some disks start to build at redshift  $z \sim 5$ , they grow slowly ( $\tau_d \sim 1$  Gyr) due to violent disk instabilities and clump migration, which result in a low cold gas fraction available in the outskirts of these systems or a

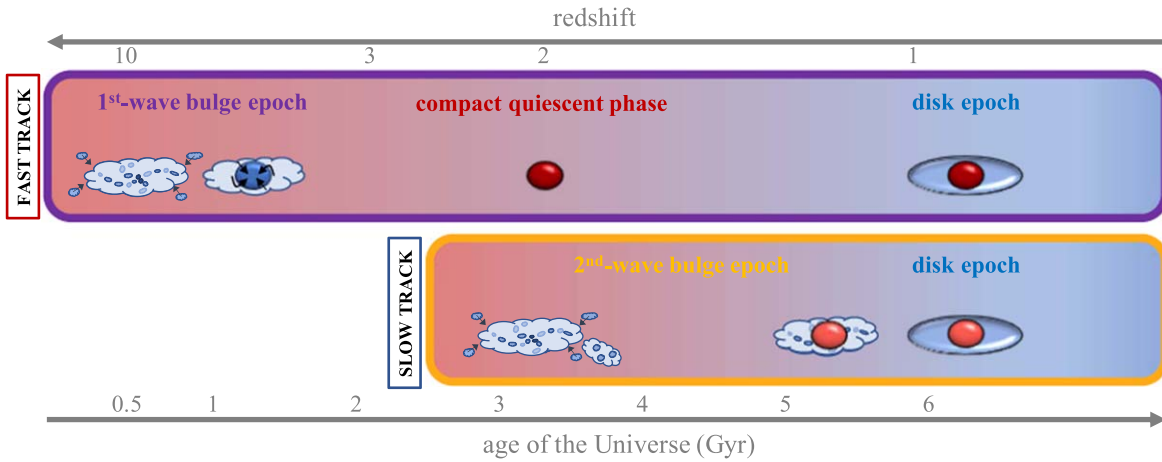


**Figure 10.** Illustration of the proposed scenario for the formation and morphological evolution of massive disk galaxies at redshift  $0.14 < z \leq 1$ . This cartoon complements the picture detailed in Paper I (Figure 13), adding the information about the disk growth. The upper panel shows the evolution of fast-track systems. These galaxies build a compact spheroid at high redshift through an intense episode of star formation (first-wave bulge), evolve rapidly through a blue and red nugget phase ( $z \sim 1.5\text{--}3$ ), and grow an extended stellar disk by redshift  $z \sim 1$ . The lower panel shows the evolution of slow-track systems. In these galaxies, there is a high level of (slow) coevolution between the spheroidal (second-wave bulge;  $z < 3$ ) and disk component ( $z \sim 1$ ), and probably no compact quiescent phase would be observed; i.e., a relatively prominent star-forming disk is always present. In the cartoon, the difference in age between first- and second-wave bulges is marked by darker to lighter red in the disk galaxies sketched at redshift  $z < 1$ .

lower efficiency of star formation. Similarly, the star formation in disks around second-wave bulges may be lower because the recent growth of the bulge has depleted the cold gas in the outskirts of the galaxy. In the New Horizon cosmological simulations, the driver of the bulge growth in disk-dominated galaxies is the increase of perturbed disk stars at early cosmic time until  $z \sim 1.5$  (Park et al. 2019), which results in a lower efficiency for the formation of stars in the disk. Again, this migration of stars from an unstable primordial disk into a compact spheroid agrees with the compaction events that are responsible for forming red nugget systems (Ceverino et al. 2015; Zolotov et al. 2015).

Several studies described the inside-out growth of massive galaxies by studying the radial gradient of their stellar mass surface density (e.g., van Dokkum et al. 2010; Patel et al. 2013). By linking the progenitors and descendants of these galaxies, these works show that massive galaxies have assembled their extended stellar halos around compact and dense cores. Similarly, the observed size evolution of star-forming galaxies was interpreted as a different distribution of their stellar populations, where the youngest stars have a more extended distribution than the older stars (e.g., Williams et al. 2010). Our analysis adds a fundamental piece of information to these studies: we morphologically separate the bulge and disk components and derive their stellar population properties, providing clues about the assembly time for each component separately.

Interestingly, we find that not only do galaxies form in a downsizing fashion, each of their morphological components does also. As shown in Figures 5 and 6, galaxies, bulges, and disks form their stars later, as they are less massive. Interestingly, more massive systems are not only older but also more compact.

We find that the inside-out growth of massive disk galaxies strongly depends on the bulge mass (see Figure 6), which actually drives the morphological evolution of our galaxies. Our results complement and extend (up to redshift  $z \sim 1$ ) the results obtained by Méndez-Abreu et al. (2021) studying the evolution of bulges and disks in local galaxies within the

CALIFA survey (Sánchez et al. 2012). The properties of bulges drive the future evolution of the galaxy as a whole, while disks have properties being set up by those of the galaxy but not affecting them.

## 5. Conclusions

In this work, we have investigated how massive disk galaxies shape their morphology across cosmic time. We studied a sample of galaxies from the SHARDS spectrophotometric survey in GOODS-N, which we photometrically modeled as a central bulge and an extended stellar disk. Thanks to the SHARDS data and the exquisite morphological information provided by the HST/CANDELS data, we retrieved the SEDs of each bulge and disk in those galaxies with a spectral resolution  $R \sim 50$ . The spectral resolution and depth of the SHARDS data allowed us to characterize the individual SFHs fitting the SEDs to stellar population synthesis models.

We find that the majority ( $\sim 85\%$ ) of massive disk galaxies grow inside-out. The peak in the formation of bulges in massive galaxies at  $0.14 < z \leq 1$  occurred at  $\bar{z}_{M,b} = 1.6$ , with a first-wave population building half of its mass as early as 0.9 Gyr after the big bang ( $\bar{z}_{M,b} = 6.2$ ) and a second wave peaking 3.8 Gyr later ( $\bar{z}_{M,b} = 1.3$ ). In contrast, the disks in these galaxies typically formed at  $\bar{z}_{M,d} = 1$ . The bulges formed in a first wave at earlier cosmic times took longer (5.2 Gyr) to grow a disk than the bulges in the second wave (which took 0.7 Gyr), with many of the latter still showing significant star formation activity in their disks.

There are a few disks ( $\sim 15\%$ ) that started to assemble as early as first-wave bulges ( $z \gtrsim 3$ ), but they grow on longer timescales ( $\tau_d \gtrsim 1$  Gyr) compared to bulges ( $\tau_b \lesssim 300$  Myr). Similarly, second-wave disks also assemble on longer timescales, suggesting a higher degree of coevolution between the bulge and disk components in galaxies at redshift  $z \lesssim 1.5$  compared to higher-redshift ones. The average rate of star formation for disks that develop around first-wave bulges could be two to three times more intense than that of disks around second-wave bulges.

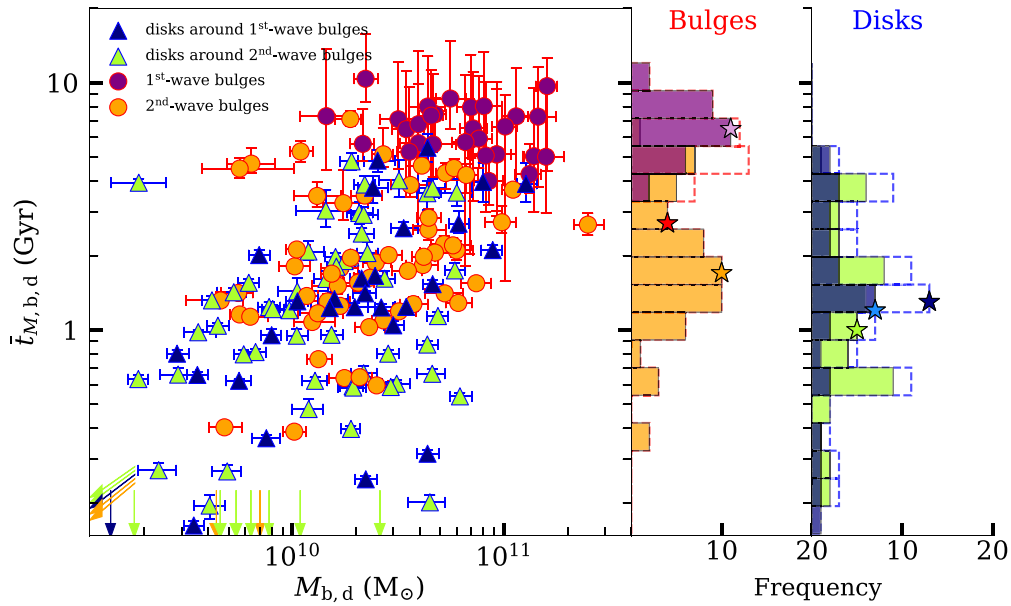


**Figure 11.** Mass-weighted stellar ages of bulges (dots) and disks (triangles) as a function of their stellar mass. Purple and blue symbols stand for first-wave bulges ( $\bar{z}_{M,b} > 3$ ) and the disks around them, while orange and green symbols represent second-wave bulges ( $\bar{z}_{M,b} < 3$ ) and the disks around them. Errors are reported as the 16th–84th percentile interval. Arrows mark upper limits for bulges and disks with mass-weighted ages  $\bar{t}_M < 150$  Myr. Purple and orange histograms stand for first- and second-wave bulges, while the red dashed histogram stands for the entire bulge population. Blue and green histograms stand for disks around first- and second-wave bulges, while the blue dashed histogram stands for the entire disk population. The median values of each distribution are marked with stars.

Importantly, we find that not only do galaxies grow in a downsizing fashion, each of their morphological components does also. Both older disks and older bulges are more massive than younger stellar structures. In addition, the oldest and most massive bulges and disks are also the most compact ones.

Accordingly with the latest results on the formation of nearby disk galaxies from Méndez-Abreu et al. (2021), we find that the mass of the bulge regulates the timing of the growth of the extended stellar disk. In particular, galaxies hosting the more compact (first-wave) bulges took longer to acquire their disks than galaxies containing second-wave bulges. But we do not find distinct physical properties (e.g., mass, star formation timescale, mass surface density, and Sérsic index) for the disks in both types of galaxies. Thus, since disks consistently form at  $z \sim 1$  around first- and second-wave bulges, we conclude that the only way to distinguish the formation mechanisms of these galaxies is to disentangle the SFHs of their disks from those of bulges. Indeed, the mechanisms that drive the formation of massive disk galaxies left imprints on the observed properties of their first- and second-wave bulges.

We would like to thank the anonymous referee for improving the content of the manuscript. We are grateful to Ignacio Trujillo and Christopher J. Conselice for the useful discussions and comments. L.C. wishes to thank Cristina Cabello for the support provided while this project was devised and Michele Perna for the fruitful discussions. L.C. acknowledges financial support from Comunidad de Madrid under Atacción de Talento grant 2018-T2/TIC-11612. L.C. and P.G. P.G. acknowledge support from the Spanish Ministerio de Ciencia, Innovación y Universidades through grant PGC2018-093499-B-I00. J.M.A. acknowledges the support of the Viera y Clavijo Senior program funded by ACIISI and ULL. D.C. is a Ramon-Cajal Researcher and supported by the Ministerio de Ciencia, Innovación y Universidades (MICIU/FEDER) under research grant PGC2018-094975-C21. This work has made use

of the Rainbow Cosmological Surveys Database, which is operated by the Centro de Astrobiología (CAB/INTA), partnered with the University of California Observatories at Santa Cruz (UCO/Lick, UCSC).

### Appendix Mass-weighted Ages

In this Appendix, we directly compare the age distributions of each bulge and disk, explicitly showing what we claimed in Sections 3.1 and 3.2: on average, bulges are older than disks (Figure 11). Bulges have median mass-weighted ages  $\bar{t}_{M,b} = 2.7^{+3.9}_{-1.6}$  Gyr, while disks present  $\bar{t}_{M,d} = 1.2^{+1.6}_{-0.9}$  Gyr. This means that, on average, spheroidal galaxies take  $\sim 1.5$  Gyr to acquire a stellar disk (see Section 3.3.2). In Paper I, we found that 48% of our bulges have  $\bar{t}_{M,b} > 3$  Gyr. In contrast, only 14% of disks have  $\bar{t}_{M,d} > 3$  Gyr. At the redshift of observation, 7% of bulges and 23% of disks present significant ongoing star formation and/or assembly activity ( $\bar{t}_M < 500$  Myr).

We find that first-wave bulges have  $\bar{t}_{M,b} = 6.5^{+1.5}_{-1.4}$  Gyr, while the disks around them present a median  $\bar{t}_{M,d} = 1.3^{+1.8}_{-0.9}$  Gyr. On the other hand, second-wave bulges have a median  $\bar{t}_{M,b} = 1.7^{+2.0}_{-0.8}$  Gyr, while the disks around them are  $1.0^{+1.7}_{-0.8}$  Gyr old.

### ORCID iDs

Luca Costantin <https://orcid.org/0000-0001-6820-0015>  
Pablo G. Pérez-González <https://orcid.org/0000-0003-4528-5639>  
Jairo Méndez-Abreu <https://orcid.org/0000-0002-8766-2597>  
Marc Huertas-Company <https://orcid.org/0000-0002-1416-8483>  
Belén Alcalde Pampliega <https://orcid.org/0000-0002-4140-0428>

Marc Balcells  <https://orcid.org/0000-0002-3935-9235>  
 Guillermo Barro  <https://orcid.org/0000-0001-6813-875X>  
 Daniel Ceverino  <https://orcid.org/0000-0002-8680-248X>  
 Helena Domínguez Sánchez  <https://orcid.org/0000-0002-9013-1316>  
 Néstor Espino-Briones  <https://orcid.org/0000-0001-6426-3844>  
 Anton M. Koekemoer  <https://orcid.org/0000-0002-6610-2048>

## References

- Athanassoula, E. 2005, *MNRAS*, **358**, 1477  
 Barro, G., Faber, S. M., Pérez-González, P. G., et al. 2013, *ApJ*, **765**, 104  
 Barro, G., Pérez-González, P. G., Cava, A., et al. 2019, *ApJS*, **243**, 22  
 Belli, S., Newman, A. B., & Ellis, R. S. 2019, *ApJ*, **874**, 17  
 Bournaud, F., Elmegreen, B. G., & Elmegreen, D. M. 2007, *ApJ*, **670**, 237  
 Brook, C. B., Kawata, D., Martel, H., Gibson, B. K., & Bailin, J. 2006, *ApJ*, **639**, 126  
 Bruce, V. A., Dunlop, J. S., McLure, R. J., et al. 2014, *MNRAS*, **444**, 1660  
 Bruzual, G., & Charlot, S. 2003, *MNRAS*, **344**, 1000  
 Buitrago, F., Trujillo, I., Conselice, C. J., & Häußler, B. 2013, *MNRAS*, **428**, 1460  
 Calzetti, D., Armus, L., Bohlin, R. C., et al. 2000, *ApJ*, **533**, 682  
 Carnall, A. C., McLure, R. J., Dunlop, J. S., et al. 2019, *MNRAS*, **490**, 417  
 Ceverino, D., Dekel, A., Tweed, D., & Primack, J. 2015, *MNRAS*, **447**, 3291  
 Ceverino, D., Klessen, R. S., & Glover, S. C. O. 2018, *MNRAS*, **480**, 4842  
 Chabrier, G. 2003, *PASP*, **115**, 763  
 Clauwens, B., Schaye, J., Franx, M., & Bower, R. G. 2018, *MNRAS*, **478**, 3994  
 Cole, S., Lacey, C. G., Baugh, C. M., & Frenk, C. S. 2000, *MNRAS*, **319**, 168  
 Costantin, L., Corsini, E. M., Méndez-Abreu, J., et al. 2018a, *MNRAS*, **481**, 3623  
 Costantin, L., Méndez-Abreu, J., Corsini, E. M., et al. 2017, *A&A*, **601**, A84  
 Costantin, L., Méndez-Abreu, J., Corsini, E. M., et al. 2018b, *A&A*, **609**, A132  
 Costantin, L., Méndez-Abreu, J., Corsini, E. M., et al. 2020, *ApJL*, **889**, L3  
 Costantin, L., Pérez-González, P. G., Méndez-Abreu, J., et al. 2021, *ApJ*, **913**, 125  
 Crain, R. A., Schaye, J., Bower, R. G., et al. 2015, *MNRAS*, **450**, 1937  
 Dalcanton, J. J., Spergel, D. N., & Summers, F. J. 1997, *ApJ*, **482**, 659  
 Damjanov, I., McCarthy, P. J., Abraham, R. G., et al. 2009, *ApJ*, **695**, 101  
 de la Rosa, I. G., La Barbera, F., Ferreras, I., et al. 2016, *MNRAS*, **457**, 1916  
 de Lorenzo-Cáceres, A., Méndez-Abreu, J., Thorne, B., & Costantin, L. 2019a, *MNRAS*, **484**, 665  
 de Lorenzo-Cáceres, A., Sánchez-Blázquez, P., Méndez-Abreu, J., et al. 2019b, *MNRAS*, **484**, 5296  
 Dekel, A., & Burkert, A. 2014, *MNRAS*, **438**, 1870  
 Dekel, A., Lapiner, S., Ginzburg, O., et al. 2020, *MNRAS*, **496**, 5372  
 Dekel, A., Sari, R., & Ceverino, D. 2009, *ApJ*, **703**, 785  
 Dimauro, P., Huertas-Company, M., Daddi, E., et al. 2018, *MNRAS*, **478**, 5410  
 Domínguez Sánchez, H., Pérez-González, P. G., Esquej, P., et al. 2016, *MNRAS*, **457**, 3743  
 Domínguez-Palmero, L., & Balcells, M. 2008, *A&A*, **489**, 1003  
 Domínguez-Palmero, L., & Balcells, M. 2009, *ApJL*, **694**, L69  
 Dubois, Y., Beckmann, R., Bournaud, F., et al. 2021, *A&A*, **651**, A109  
 Eggen, O. J., Lynden-Bell, D., & Sandage, A. R. 1962, *ApJ*, **136**, 748  
 El-Badry, K., Quataert, E., Wetzell, A., et al. 2018, *MNRAS*, **473**, 1930  
 Estrada-Carpenter, V., Papovich, C., Momcheva, I., et al. 2019, *ApJ*, **870**, 133  
 Estrada-Carpenter, V., Papovich, C., Momcheva, I., et al. 2020, *ApJ*, **898**, 171  
 Fall, S. M., & Efstathiou, G. 1980, *MNRAS*, **193**, 189  
 Flores-Freitas, R., Chies-Santos, A. L., Furlanetto, C., et al. 2022, *MNRAS*, **512**, 245  
 Freeman, K. C. 1970, *ApJ*, **160**, 811  
 Gadotti, D. A., Bittner, A., Falcón-Barroso, J., et al. 2020, *A&A*, **643**, A14  
 Gao, H., Ho, L. C., Barth, A. J., & Li, Z.-Y. 2020, *ApJS*, **247**, 20  
 Graham, A. W. 2013, in *Planets, Stars and Stellar Systems*, ed. T. D. Oswalt & W. C. Keel, Vol. 6 (Berlin: Springer), 91  
 Graham, A. W., & Driver, S. P. 2005, *PASA*, **22**, 118  
 Grogin, N. A., Kocevski, D. D., Faber, S. M., et al. 2011, *ApJS*, **197**, 35  
 Heavens, A., Panter, B., Jimenez, R., & Dunlop, J. 2004, *Natur*, **428**, 625  
 Hopkins, P. F., Cox, T. J., Younger, J. D., & Hernquist, L. 2009a, *ApJ*, **691**, 1168  
 Hopkins, P. F., Kereš, D., Oñorbe, J., et al. 2014, *MNRAS*, **445**, 581  
 Hopkins, P. F., Somerville, R. S., Cox, T. J., et al. 2009b, *MNRAS*, **397**, 802  
 Hsu, L.-T., Lin, L., Dickinson, M., et al. 2019, *ApJ*, **871**, 233  
 Huang, S., Ho, L. C., Peng, C. Y., Li, Z.-Y., & Barth, A. J. 2013a, *ApJ*, **766**, 47  
 Huang, S., Ho, L. C., Peng, C. Y., Li, Z.-Y., & Barth, A. J. 2013b, *ApJL*, **768**, L28  
 Hubble, E. P. 1926, *ApJ*, **64**, 321  
 Koekemoer, A. M., Faber, S. M., Ferguson, H. C., et al. 2011, *ApJS*, **197**, 36  
 Kormendy, J. 2016, in *Astrophysics and Space Science Library, Elliptical Galaxies and Bulges of Disc Galaxies: Summary of Progress and Outstanding Issues*, ed. E. Laurikainen, R. Peletier, & D. Gadotti, Vol. 418 (Switzerland: Springer International), 431  
 Kormendy, J., & Kennicutt, R. C. J. 2004, *ARA&A*, **42**, 603  
 Larson, R. B. 1976, *MNRAS*, **176**, 31  
 Lilly, S. J., Le Fevre, O., Hammer, F., & Crampton, D. 1996, *ApJL*, **460**, L1  
 Madau, P., & Dickinson, M. 2014, *ARA&A*, **52**, 415  
 Madau, P., Ferguson, H. C., Dickinson, M. E., et al. 1996, *MNRAS*, **283**, 1388  
 Mancini, C., Daddi, E., Juneau, S., et al. 2019, *MNRAS*, **489**, 1265  
 Margalef-Bentabol, B., Conselice, C. J., Mortlock, A., et al. 2016, *MNRAS*, **461**, 2728  
 Margalef-Bentabol, B., Conselice, C. J., Mortlock, A., et al. 2018, *MNRAS*, **473**, 5370  
 Méndez-Abreu, J., Aguerri, J. A. L., Corsini, E. M., & Simonneau, E. 2008, *A&A*, **478**, 353  
 Méndez-Abreu, J., de Lorenzo-Cáceres, A., & Sánchez, S. F. 2021, *MNRAS*, **504**, 3058  
 Méndez-Abreu, J., Debattista, V. P., Corsini, E. M., & Aguerri, J. A. L. 2014, *A&A*, **572**, A25  
 Méndez-Abreu, J., Sánchez, S. F., & de Lorenzo-Cáceres, A. 2019a, *MNRAS*, **484**, 4298  
 Méndez-Abreu, J., Sánchez, S. F., & de Lorenzo-Cáceres, A. 2019b, *MNRAS*, **488**, L80  
 Méndez-Abreu, J., Simonneau, E., Aguerri, J. A. L., & Corsini, E. M. 2010, *A&A*, **521**, A71  
 Mo, H. J., Mao, S., & White, S. D. M. 1998, *MNRAS*, **295**, 319  
 Morelli, L., Corsini, E. M., Pizzella, A., et al. 2015, *MNRAS*, **452**, 1128  
 Morelli, L., Pannigiani, M., Corsini, E. M., et al. 2016, *MNRAS*, **463**, 4396  
 Morishita, T., Abramson, L. E., Treu, T., et al. 2019, *ApJ*, **877**, 141  
 Naab, T., Johansson, P. H., & Ostriker, J. P. 2009, *ApJL*, **699**, L178  
 Nelson, D., Pillepich, A., Springel, V., et al. 2018, *MNRAS*, **475**, 624  
 Noguchi, M. 1999, *ApJ*, **514**, 77  
 Oser, L., Ostriker, J. P., Naab, T., Johansson, P. H., & Burkert, A. 2010, *ApJ*, **725**, 2312  
 Park, M.-J., Yi, S. K., Dubois, Y., et al. 2019, *ApJ*, **883**, 25  
 Patel, S. G., van Dokkum, P. G., Franx, M., et al. 2013, *ApJ*, **766**, 15  
 Pérez-González, P. G., Cava, A., Barro, G., et al. 2013, *ApJ*, **762**, 46  
 Pérez-González, P. G., Gil de Paz, A., Zamorano, J., et al. 2003, *MNRAS*, **338**, 525  
 Pérez-González, P. G., Rieke, G. H., Villar, V., et al. 2008, *ApJ*, **675**, 234  
 Pfeffer, J., Bekki, K., Couch, W. J., Koribalski, B. S., & Forbes, D. A. 2022, *MNRAS*, **511**, 1072  
 Pillepich, A., Nelson, D., Hernquist, L., et al. 2018, *MNRAS*, **475**, 648  
 Sánchez, S. F., Kennicutt, R. C., Gil de Paz, A., et al. 2012, *A&A*, **538**, A8  
 Schaye, J., Crain, R. A., Bower, R. G., et al. 2015, *MNRAS*, **446**, 521  
 Sérsic, J. L. 1968, *Atlas de Galaxias Australes* (Cordoba: Observatorio Astronómico)  
 Steinmetz, M., & Navarro, J. F. 2002, *NewA*, **7**, 155  
 Suess, K. A., Kriek, M., Price, S. H., & Barro, G. 2021, *ApJ*, **915**, 87  
 Tacchella, S., Conroy, C., Faber, S. M., et al. 2022, *ApJ*, **926**, 134  
 Tacchella, S., Diemer, B., Hernquist, L., et al. 2019, *MNRAS*, **487**, 5416  
 van Dokkum, P. G., Whitaker, K. E., Brammer, G., et al. 2010, *ApJ*, **709**, 1018  
 Williams, R. J., Quadri, R. F., Franx, M., et al. 2010, *ApJ*, **713**, 738  
 Zolotov, A., Dekel, A., Mandelker, N., et al. 2015, *MNRAS*, **450**, 2327